Capabilities of dual-frequency millimeter wave SAR with monopulse processing for ground moving target indication

Rüegg, M ; Meier, E ; Nüesch, D

Abstract: Ground moving target indication (GMTI) for syn- thetic aperture radar (SAR) provides information on nonstatic objects in radar imagery of a static ground scene. An efficient approach for GMTI is the use of multichannel SAR systems for a space- and time-variant analysis of moving targets. This allows the indication, correction of position displacement, and estimation of radial velocity components of moving targets in a SAR image. All three steps are possible due to a determinable Doppler frequency shift in the radar signal caused by radial target movement. This paper focuses on the millimeter wave (mmW) SAR system MEMPHIS with multichannel amplitude-comparison monopulse data acquisition and the ability to use carrier frequencies of 35 and 94 GHz simultaneously, making it a dual-frequency SAR. This paper includes mmW-specific SAR GMTI considerations, an adaptive algorithm to collect velocity and position information on moving targets with mmW monopulse radar, and a discussion on GMTI blind speed elimination and target velocity ambiguity resolving by dual-frequency SAR. To determine the capabilities of both, system and algorithm, three large-scale experiments with MEMPHIS in different environments are presented.

DOI: https://doi.org/10.1109/TGRS.2006.888464

Capabilities of Dual-Frequency Millimeter Wave SAR With Monopulse Processing for Ground Moving Target Indication

Maurice Rüegg, *Student Member, IEEE*, Erich Meier, and Daniel Nüesch, *Member, IEEE*

***Abstract*—Ground moving target indication (GMTI) for synthetic aperture radar (SAR) provides information on nonstatic objects in radar imagery of a static ground scene. An efficient approach for GMTI is the use of multichannel SAR systems for a space- and time-variant analysis of moving targets. This allows the indication, correction of position displacement, and estimation of radial velocity components of moving targets in a SAR image. All three steps are possible due to a determinable Doppler frequency shift in the radar signal caused by radial target movement. This paper focuses on the millimeter wave (mmW) SAR system MEMPHIS with multichannel amplitude-comparison monopulse data acquisition and the ability to use carrier frequencies of 35 and 94 GHz simultaneously, making it a dual-frequency SAR. This paper includes mmW-specific SAR GMTI considerations, an adaptive algorithm to collect velocity and position information on moving targets with mmW monopulse radar, and a discussion on GMTI blind speed elimination and target velocity ambiguity resolving by dual-frequency SAR. To determine the capabilities of both, system and algorithm, three large-scale experiments with MEMPHIS in different environments are presented.**

***Index Terms*—Ground moving target indication (GMTI), millimeter wave (mmW) radar, monopulse radar, synthetic aperture radar (SAR).**

I. Introduction

THE EFFECTS of smearing, defocus, and displacement of moving targets in synthetic aperture radar (SAR) imagery have long been known and are discussed in detail in [1]. Ground moving target indication (GMTI) with SAR has been a widely explored field of interest ever since. Techniques for detection, position correction, refocusing, and velocity measurements of moving targets include the use of single- as well as multichannel SAR data. They cover a wide range of topics from simple multilooking [2] to displaced-phase-center antenna processing [2], [3], polarimetric data analysis [4], along-track interferometry (ATI) [5], [6], monopulse processing [2], and space time adaptive processing [6]–[8].

Using a millimeter wave (mmW) SAR sensor for GMTI experiments has several advantages as well as drawbacks. Among the advantages are the relatively small size of the sensor antenna and hardware—suitable for application in ultralight aircraft and unmanned aerial vehicles—and a high GMTI sensitivity because of the short wavelength. The usually very small synthetic aperture of mmW SAR reduces target smearing and defocus, especially at high target velocities. This is discussed in detail in Section II. The main drawbacks are the short signal range due to tropospheric attenuation at these wavelengths, high target Doppler values due to high carrier frequencies resulting in small unambiguous target velocity measurements, and extremely short baselines in interferometric applications that may make ATI impractical as shown in Section III. Section IV discusses how a dual-frequency approach is able to resolve target Doppler ambiguities.

Monopulse processing for GMTI is often used as an equivalent to ATI in the SAR community [9]. In this paper, a distinction is made in that ATI refers to interferometric SAR (InSAR) and the direct comparison of two or more received data records [5] from multiple antennas while monopulse or $\Sigma\Delta$ processing is a general term often used for tracking radar systems and always specified through a sum data signal and one or more isochronous difference data signals [10]. Monopulse processing looks at the complex ratios between these multiple signals and is well suited for GMTI. In Section V, an algorithm for mmW monopulse SAR processing, whose outline was first presented in [11], is given and discussed.

In Section VI, we show results from three experiments with the airborne mmW SAR MEMPHIS [12]. An airfield offered an ideal controlled environment for a first experiment under almost ideal but realistic conditions, with multiple targets and a straight target path on the airfield runway, two different but constant target velocities, and an open, low-clutter view of the scene from the SAR. From the experiment, frequency spectra, processed SAR images with position-corrected moving targets, and accurate target velocities and positions are presented. To verify the developed algorithm, differential geographical positioning systems (dGPS) measurements of all target positions and movements were recorded during the experiment and compared to the GMTI results.

A second experiment compares dGPS measurements to SAR GMTI results for slow-moving targets on a field path. Three vehicles of the same type as in the first experiment were used. Environment conditions were far from ideal with a twisting target path, clutter from trees, fields, and rocks, and nonconstant target velocities. Third, data collected from targets of opportunity on a freeway show the potential for fast-moving target indication with mmW SAR.

Finally, we draw our conclusions in Section VII.

Manuscript received July 25, 2006; revised October 11, 2006. This work was supported by the Procurement and Technology Center of the Swiss Federal Department of Defense (armasuisse).

The authors are with the Remote Sensing Laboratories, University of Zurich, CH-8006 Zurich, Switzerland (e-mail: mrueegg@geo.unizh.ch).

Digital Object Identifier 10.1109/TGRS.2006.888464

II. Moving Target Effects

A mmW SAR system has some advantages as well as disadvantages when it comes to the imaging of moving targets. Because of the very short wavelength, we have a high signal phase sensitivity for even small target velocities. This effect may be observed as a Doppler shift f_d in the received signal of a target moving with a radial velocity v_r as

$$f_\mathrm{d} = \frac{2v_\mathrm{r}}{\lambda_\mathrm{c}} \tag{1}$$

where λ_c is the wavelength of the carrier signal. Unfortunately, f_d may easily become aliased when larger than the limit determined by the system pulse repetition frequency (PRF), resulting in a possibly ambiguous measured target velocity

$$v_\mathrm{r} = \frac{(f_\mathrm{d} + n \cdot \mathrm{PRF})\lambda_\mathrm{c}}{2} \qquad \text{for all } n \in \mathbb{Z}. \tag{2}$$

This ambiguity may be resolved by additional information, such as using dual-frequency SAR (see Section IV).

A direct effect of (1) is the displacement d of moving targets in a SAR image as given by [1], [13]

$$d = \frac{v_\mathrm{r}}{v_\mathrm{s}} \cdot R \tag{3}$$

where v_s is the cross-range (azimuth) SAR platform speed and R the range to the target. Since R is changing over the radar dwell time t, target displacement may be smeared. The advantage of a mmW SAR is its antenna aperture in azimuth that is generally very small. This implies that t is short for any given target and displacement variations are small.

Furthermore, [1] states range smearing of a moving target over multiple range resolution cells when

$$v_\mathrm{r} t \geq \rho_\mathrm{r} \tag{4}$$

where ρ_r is the range resolution. A short time t is again of advantage. However, ρ_r may be in the order of centimeters for a large bandwidth, high-resolution mmW SAR which reduces the advantage of a small value for t.

Another effect is the defocus of moving targets, depending on azimuth target velocity v_z and range acceleration a_r. As stated in [1], defocusing appears if we have

$$\frac{2\pi}{\lambda_\mathrm{c} R(t)} \left| \left(1 - \frac{v_\mathrm{z}}{v_\mathrm{s}}\right)^2 - \frac{a_\mathrm{r} R_0}{v_\mathrm{s}} - 1 \right| (v_\mathrm{s} t)^2 \geq \pi \tag{5}$$

where R_0 is the range of closest approach to the target. Because λ_c is small in a mmW SAR, (5) may often be true even for small target azimuth velocities or range accelerations.

Regarding (3)–(5), an interesting point is that for a target T moving at a constant velocity perpendicular to the sensor track with v_T, we have $v_\mathrm{r} = v_T$ while $v_\mathrm{z} = 0$ and $a_\mathrm{r} = 0$. However, this is only true at R_0. At all other points in the aperture, we get

$$v_\mathrm{r}(t) = v_T \cdot \cos\varphi(t) \tag{6}$$

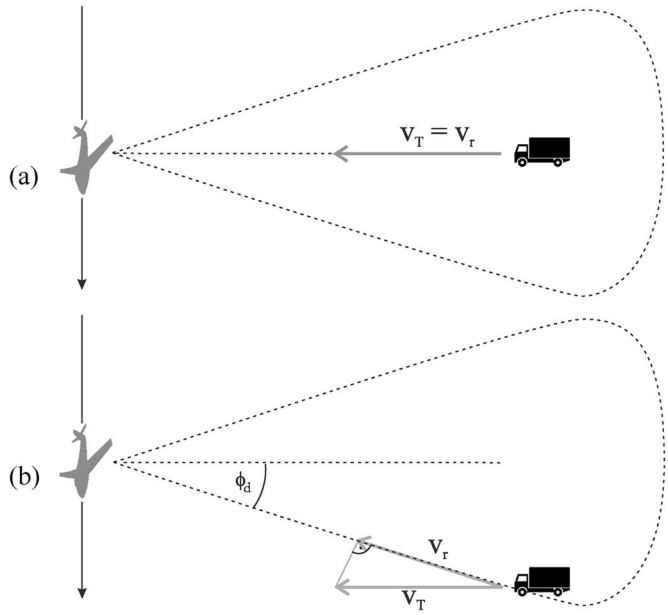

Fig. 1. SAR geometry with a target moving perpendicular to the flight track with v_T. (a) At beam center, the target velocity is only radial. (b) Out of beam center, the target velocity has a radial as well as a tangential component.

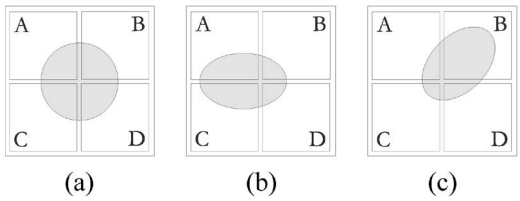

Fig. 2. Monopulse concept with a target seen by four independent receive channels A to D. In (a), the target is at boresight. In (b) and (c), it is displaced.

with the target aspect angle $\varphi(t) \in [-\phi_\mathrm{d}, \phi_\mathrm{d}]$, where ϕ_d is the antenna aperture divergence angle, and

$$v_\mathrm{z}(t) = v_T \cdot \sin\varphi(t). \tag{7}$$

Additionally, because φ changes with t, we have

$$a_\mathrm{r}(t) = \frac{d}{dt} v_\mathrm{r}(t) = \frac{d}{dt} \left(\cos\varphi(t)\right). \tag{8}$$

This means that even for a target moving perpendicular to the SAR flight track with constant v_T, and although ϕ_d is very small for mmW SAR, (5) may cause a target defocus over the synthetic aperture. Fig. 1 illustrates this phenomenon.

III. Monopulse SAR

A monopulse radar has a sum signal Σ and multiple isochronous difference signals Δ. They are the result of two, four or more separate channels sending the same radio signal at the same time (hence the term monopulse), but receiving ground return echoes independently. While Σ is the sum signal of echoes from all channels, Δ is formed from the differences thereof. These differences in amplitude as well as phase come from different viewing angles or, in the case of moving targets in SAR, from different angle-dependent Doppler frequency shifts. Fig. 2 shows a schematic view of a monopulse system

with four channels A, B, C, D. In (a), the difference signal will be equal to zero, meaning a target at boresight while (b) and (c) show targets that are displaced in either azimuth or both azimuth and elevation. For a tracking radar using monopulse, these off-center signals may translate directly into a correction angle [10]. For a SAR, this is equal to a Doppler frequency behavior in the signals that is different from static clutter as explained below.

If we assume a physical antenna receiver channel arrangement as in Fig. 2, we may express the sum and difference signals in azimuth and elevation as

$$\Sigma = A + B + C + D \tag{9}$$
$$\Delta_{\mathrm{az}} = (A + C) - (B + D) \tag{10}$$
$$\Delta_{\mathrm{el}} = (A + B) - (C + D). \tag{11}$$

Measurable frequency shifts in a mmW SAR are only present in the Doppler domain (target displacement in azimuth) and not in the range domain (elevation) where the difference in the magnitude between carrier frequency and Doppler shift is very large [1]. The elevation difference signal Δ_{el} does not play any important role and will be ignored in the following. Hence, when referring to Δ we will always mean the azimuth difference Δ_{az}.

Once we form the signal monopulse ratio [10] defined as

$$\mathrm{MPR} = \frac{\Delta}{\Sigma} \tag{12}$$

we will get zero for all boresight echoes of static targets of zero Doppler frequency, a distinct monopulse curve M from all other echoes as a function of Doppler frequency, and moving targets deviating from this curve.

A. Phase and Amplitude Comparison

There are two different kinds of monopulse radars.

1) Amplitude-comparison monopulse consists of multiple (horn) antennas in a parabolic reflector and a single lens bundling the individual signals and giving them a common phase center. The resulting look directions of the receive channels are squinted away from each other by an angle φ_0.
2) Phase-comparison monopulse uses multiple separate antennas looking all in the same direction with a separation baseline B resulting in independent phase centers.

The two concepts are illustrated in Fig. 3. The idea of phase-comparison monopulse is commonly used in InSAR applications. However, mmW SAR systems often rely on amplitude-comparison monopulse because the physical baseline B often becomes very small and hard to be practically realizable for GMTI applications. For example, measurements of radial target velocities v_{r} from 5 to 20 m/s at a wavelength λ_{c} of 4 mm would result in a baseline of only 4 to 1 cm as calculated using

$$B = \frac{\lambda_{\mathrm{c}}}{2}\frac{v_{\mathrm{s}}}{v_{\mathrm{r}}} \tag{13}$$

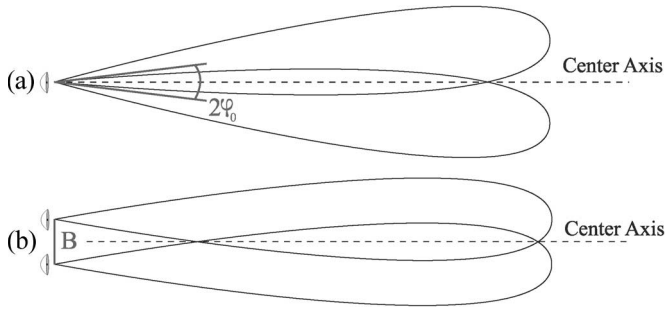

Fig. 3. (a) Amplitude-comparison monopulse with one phase center and two squinted beams. (b) Phase-comparison monopulse with two phase centers, parallel beams, and a separation baseline.

and assuming an airborne SAR platform velocity in azimuth v_{s} of 100 m/s. (13) results with the assumption of a phase difference between physical channels equal to $\lambda_{\mathrm{c}}/2$. The time difference between the antenna phase centers at the same position is $t = B/v_{\mathrm{s}}$ and during that time, a target will move a distance $v_{\mathrm{r}} \cdot t$ equal to $\lambda_{\mathrm{c}}/2$.

B. MEMPHIS SAR System

MEMPHIS is an experimental airborne mmW SAR developed by Forschungsgesellschaft für Angewandte Naturwissenschaften-Forschungsinstitut für Hochfrequenzphysik und Radartechnik (FGAN-FHR) [12]. Its configuration permits an amplitude-comparison monopulse mode using a setup as described in Fig. 2 to combine the signals from four independent horns arranged in a square. Ideally, the signals share a common phase center, but since the individual horns are separated locally from each other by a short distance, this is practically not completely accurate, and we will also get a small constant phase difference between channels for static targets in addition to those phase differences caused by target movement.

The system operates simultaneously at carrier frequencies of 35 and 94 GHz with two independent monopulse antennas and standard chirped signals of 200-MHz bandwidth (0.75-m sample resolution) and a PRF of 1700 Hz for each antenna. Since the Doppler frequency of a target moving with radial velocity v_{r} is given by (1) and ambiguous as stated in (2), we may receive unambiguous radial velocity measurements of up to 7.28 m/s for $f_{\mathrm{d}} \leq$ PRF at 35 GHz if the target movement direction is known and $\pm$3.64 m/s otherwise. At 94 GHz, the unambiguous velocity limit at 1700 Hz is 2.71 m/s or $\pm$1.35 m/s. All higher radial target velocities are ambiguous within the Doppler spectrum.

IV. Dual-Frequency Information

A. Theory

Ambiguous velocity measurements and, closely related blind target speeds, are two important issues that often arise when looking at ground moving targets with high-frequency SAR systems. Velocity ambiguities are due to target Doppler frequency shifts outside of the PRF and hence are aliased. Blind speeds are a special case where radial target speeds are aliased to a 0-Hz Doppler shift.

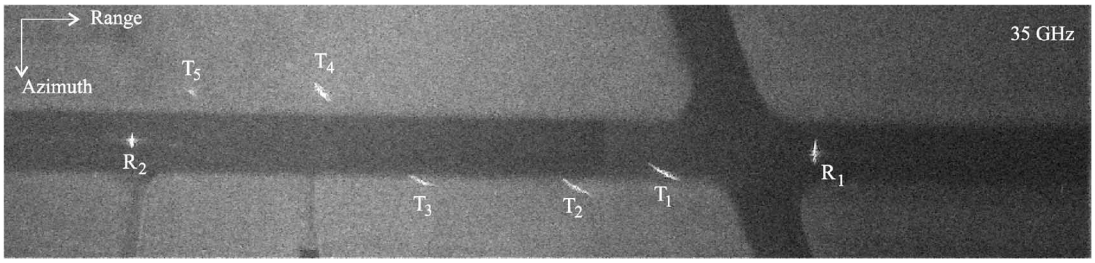

Fig. 4. Focused 35-GHz SAR image of an airfield runway. The image dimensions are 750×150 m^2 with a resolution of 0.75 m. The misplaced targets T_1 to T_5 are moving to the right. The static corner reflectors are marked as R_1 and R_2.

First, reports about exploiting dual-frequency radar to resolve Doppler ambiguities date back more than 35 years [14]. The method is to resolve Doppler shifts that are multiples of the PRF for one carrier frequency by using a second frequency where the Doppler shifts are a different multiple of the same PRF and/or aliased to a different value [15]. Hence, the problem reduces to a matter of the least common multiple. Applications for dual-frequency radar range from detection of moving targets in the presence of ground clutter to wind and storm measurements in meteorology and topographic height extraction in InSAR. Derivations of the principle include everything from dual-PRF systems [16] to dual-baseline InSAR [17].

If applying the dual-frequency technique to SAR GMTI, we are able to increase the unambiguous velocity range using the theory of least common multiples. Let us set $f_\mathrm{d} > \mathrm{PRF}$ in (1), and we get a new dual-frequency condition for Doppler ambiguities given as

$$\mathrm{PRF} < \frac{2v_\mathrm{r}}{\mathrm{lcm}(\lambda_{\mathrm{c}1}, \lambda_{\mathrm{c}2})} \tag{14}$$

where we make use of both carrier wavelengths $\lambda_{\mathrm{c}1}$ and $\lambda_{\mathrm{c}2}$ of a dual-frequency system. The operation lcm is defined as the least common multiple between two values. Unfortunately, least common multiples are only defined for integer values. $\lambda_{\mathrm{c}1}$ and $\lambda_{\mathrm{c}2}$, however, will almost never be integer values in most dual-frequency SAR systems. The solution is to define the precision of such a system. Let us say that we trust a SAR to be precise up to x decimal digits of its wavelength in meters and we may define

$$\mathrm{PRF} < \frac{2 \cdot v_\mathrm{r} \cdot 10^x}{\mathrm{lcm}\left([\lambda_{\mathrm{c}1} \cdot 10^x], [\lambda_{\mathrm{c}2} \cdot 10^x]\right)} \tag{15}$$

where $[\,]$ means the nearest integer. Hence, we just expand the fractions and round off the accuracy of velocity measurements for our system.

As an example, let us use the system parameters of MEMPHIS. At 35 GHz, we have a wavelength of $\lambda_{\mathrm{c}1} = 0.008571$ m and at 94 GHz one of $\lambda_{\mathrm{c}2} = 0.003191$ m. If we want three digits in the wavelength to be significant, we have to set x equal to 5. For a system PRF of 1700 Hz, we get a maximum unambiguous radial target velocity v_r of 2323.7 m/s since $\mathrm{lcm}(\lambda_{\mathrm{c}1} \cdot 10^5, \lambda_{\mathrm{c}2} \cdot 10^5) = \mathrm{lcm}(857, 319)$ m $= 273,383$ m. If we restrain ourselves to a lower system precision of two significant digits for the wavelength $(x = 4)$, we get $v_\mathrm{r} = 116.9$ m/s (because $\mathrm{lcm}(86, 32)$ m $= 1376$ m) which is still much larger than the unambiguous velocities for a single frequency obtained in Section III-B.

From a practical point of view, we may define a system of linear equations for a dual-frequency SAR with wavelengths $\lambda_{\mathrm{c}1}$ and $\lambda_{\mathrm{c}2}$ and measured, ambiguous target Doppler shifts $f_{\mathrm{d}1}$ and $f_{\mathrm{d}2}$

$$\begin{aligned} f_{\mathrm{d}1} &= \frac{2v_\mathrm{r}}{\lambda_{\mathrm{c}1}} - m \cdot \mathrm{PRF} \qquad \text{for all } m \in \mathbb{Z} \\ f_{\mathrm{d}2} &= \frac{2v_\mathrm{r}}{\lambda_{\mathrm{c}2}} - n \cdot \mathrm{PRF} \qquad \text{for all } n \in \mathbb{Z} \end{aligned} \tag{16}$$

Of course, this system is underdetermined with unknown true radial target velocity v_r and ambiguities m and n. If we assume (15) to be true, the system is solvable by adding (15) as a constraint to (16), depending on the system accuracy indicated by x.

This system accuracy indicated by x may be verified. Since v_r in the two equations of (16) may in practice not be the same measured value but rather $v_{\mathrm{r}1}$ and $v_{\mathrm{r}2}$, potential discrepancies between ambiguity-resolved radial target velocities $v_{\mathrm{r}1}$ measured at $\lambda_{\mathrm{c}1}$ and $v_{\mathrm{r}2}$ at $\lambda_{\mathrm{c}2}$ result in a precision indicator $\Delta\epsilon$ given as

$$\Delta\epsilon = |v_{\mathrm{r}1} - v_{\mathrm{r}2}|. \tag{17}$$

If $\Delta\epsilon$ is considerably larger than the system accuracy, we need to lower x.

B. Differences in SAR Imagery

Different ambiguous Doppler shifts $f_{\mathrm{d}1}$ and $f_{\mathrm{d}2}$ caused by moving targets in dual-frequency SAR cause differences in the focused SAR images. To illustrate this, let us look at a dual-frequency image pair of real data. In June 2004, a GMTI experiment with the MEMPHIS SAR system was realized on the runway of the airfield in Emmen, Switzerland. In this experiment, five Puch all-purpose vehicles were used as targets, with T_1 to T_3 at a nominally constant speed of 15 m/s and T_4 and T_5 at 10 m/s along the runway. Thus, they formed two independent small convoys. The front vehicle of either convoy (T_1, T_4) was equipped with a corner reflector to increase signal reception in the SAR. Two additional corner reflectors R_1 and R_2 were placed on the runway, serving as static reference targets.

The runway was imaged by MEMPHIS at 35 and 94 GHz simultaneously, with 200-MHz signal bandwidth, and a PRF of 1700 Hz. Fig. 4 shows the 750-m wide and focused Σ signal

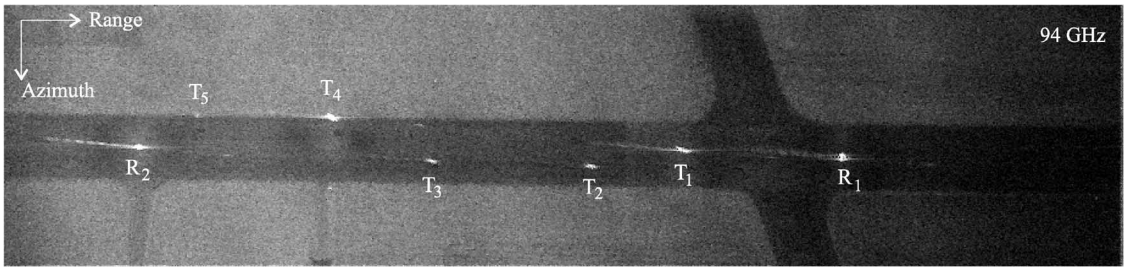

Fig. 5. Focused 94-GHz SAR image recorded simultaneously with the one in Fig. 4. Note how the moving targets T_1 to T_5 are misplaced differently here than at 35 GHz because of different Doppler shifts.

image at 35 GHz with all targets and the corner reflectors. The targets were moving from left to right, away from the SAR sensor and are vertically displaced in the image (in azimuth). Note that the targets moving more slowly (T_4, T_5) are actually displaced further away from their true position and in opposite direction in the SAR image than the ones moving more quickly (T_1 to T_3). This is exactly what may happen due to the limited PRF and aliasing in the Doppler spectrum implied by (2).

In Fig. 5, the focused Σ signal image at 94 GHz is shown as a comparison to Fig. 4. Note how the moving targets experience a different azimuth displacement than at 35 GHz. This variable shift at different carrier frequencies may even be exploited by applying change detection to the two images. One has to keep in mind, though, that objects may have different backscattering characteristics at different frequencies.

V. GMTI Processing

Independently of whether one or two carrier frequencies are available, GMTI is always possible for monopulse SAR at a single frequency—just not with unambiguous velocity determination. We developed the following $\Sigma\Delta$ algorithm to automatically indicate moving targets, get an ambiguous velocity estimation, and correct their position shifts in the SAR image. For the resolving of the true radial target velocity we are relying on the dual-frequency information.

A. Theory

While we have distinguished between amplitude- and phase-comparison monopulse methods in Section III, the data processing approach may be the same for both. Despite the misleading name, we do neither look at amplitudes nor phases in monopulse processing, but always at the complex ratios Δ/Σ. To be more exact, we define the sum signal as

$$\Sigma = |\Sigma| \cdot e^{j\phi_\Sigma} \tag{18}$$

and the difference signal as

$$\Delta = |\Delta| \cdot e^{j\phi_\Delta} \tag{19}$$

to receive the complex monopulse ratio

$$\text{MPR} = \frac{\Delta}{\Sigma} = \frac{|\Delta|}{|\Sigma|} \cdot e^{j(\phi_\Delta - \phi_\Sigma)}. \tag{20}$$

For an ideal amplitude comparison monopulse system, the receive channels share a common phase center and the phase difference $\phi_\Delta - \phi_\Sigma \equiv 0$ (see [10, Ch. 3]).

Specific to SAR, there are deviations from the general monopulse radar processing techniques described in [10, Ch. 7]. We look at the processed single-look complex signals $S_\text{c}(r, \omega)$ in the range-Doppler domain. The transformations from the received echo signal $s(t, z)$ at the antenna to the processed SAR image $s_\text{c}(r, z)$ and its equivalent in the range-Doppler domain $S_\text{c}(r, \omega)$ is

$$s(t, z) \xrightarrow{①} s_\text{c}(r, z) \xrightarrow{②} S_\text{c}(r, \omega) \tag{21}$$

where t is the fast time, r and z coordinates in range and azimuth, and ω the Doppler frequency. ① stands for the SAR processing of raw data to a single-look complex image (e.g., [18]). ② is the transformation into the range-Doppler domain given by the Fourier transform as

$$S_\text{c}(r, \omega) = \int_{-\infty}^{\infty} s_\text{c}(r, z) e^{-j\omega z} dz. \tag{22}$$

In the following, we calculate the monopulse ratio Δ/Σ for a SAR signal in the range-Doppler domain. Therefore, we do not assume a standard $\sin x/x$ radar backscattering intensity of the physical channels (e.g., [19]), but look at the Doppler frequency distribution at each range bin r as a standardized Gaussian distribution curve with a half-power frequency ω_p and a normalization constant $\alpha = 1/\omega_\text{p}$. Because the phase difference between the channels is zero, the monopulse ratio can be formed by the signal amplitudes spectra. We assume that the influence of the range r on the monopulse ratio is negligible for small image strips at large slant range distances. Hence, we define the image azimuth spectrum amplitude of the physical antenna channels independently from r as

$$|S_{\text{c}1}(\omega)| = e^{-\alpha^2(\omega+\omega_0)^2} \tag{23}$$

and

$$|S_{\text{c}2}(\omega)| = e^{-\alpha^2(\omega-\omega_0)^2}. \tag{24}$$

ω_0 is the Doppler frequency shift of the channels resulting from the squinted antenna beams with

$$\omega_0 = \frac{4\pi v_\text{s} \sin\varphi_0}{\lambda_\text{c}} \tag{25}$$

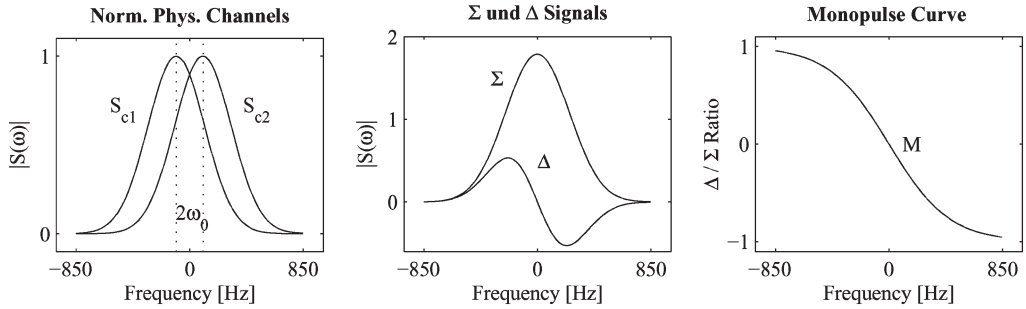

Fig. 6. Theoretical Doppler spectra of monopulse SAR. (Left) The normalized physical channels S_{c1} and S_{c2}. (Middle) The recorded monopulse signals of Σ and Δ. (Right) The monopulse curve M.

between the monopulse beams as shown in Fig. 3(a). We get the $|\Sigma|$ and $|\Delta|$ signals

$$\begin{aligned}|\Sigma(\omega)| &= |S_{c1}| + |S_{c2}| \\ &= e^{-\alpha^2(\omega+\omega_0)^2} + e^{-\alpha^2(\omega-\omega_0)^2} \\ &= e^{-\alpha^2\omega^2-\alpha^2\omega_0^2}(e^{2\alpha^2\omega\omega_0} + e^{-2\alpha^2\omega\omega_0}) \end{aligned} \tag{26}$$

and

$$\begin{aligned}|\Delta(\omega)| &= |S_{c1}| - |S_{c2}| \\ &= e^{-\alpha^2(\omega+\omega_0)^2} - e^{-\alpha^2(\omega-\omega_0)^2} \\ &= e^{-\alpha^2\omega^2-\alpha^2\omega_0^2}(e^{2\alpha^2\omega\omega_0} - e^{-2\alpha^2\omega\omega_0}). \end{aligned} \tag{27}$$

Considering the properties of the hyperbolic functions $\sinh(x) = (1/2)(e^x - e^{-x})$ and $\cosh(x) = (1/2)(e^x + e^{-x})$, we get

$$|\Sigma(\omega)| = e^{-\alpha^2(\omega^2+\omega_0^2)} \cdot 2\cosh(2\alpha^2\omega\omega_0) \tag{28}$$

and

$$|\Delta(\omega)| = e^{-\alpha^2(\omega^2+\omega_0^2)} \cdot 2\sinh(2\alpha^2\omega\omega_0). \tag{29}$$

The ideal monopulse curve of all Doppler frequencies from the static ground scene in a SAR may thus be described mathematically by a hyperbolic tangent as

$$M(\omega) = \frac{|\Delta(\omega)|}{|\Sigma(\omega)|} = \tanh(2\alpha^2\omega\omega_0). \tag{30}$$

In Fig. 6, the physical channels given by (23) and (24) are plotted on the left, analogously to the situation at the top of Fig. 3, while the sum and difference signals of (26) and (27) are shown in the center and the resulting monopulse curve of (30) on the right. For this example, a total spectrum from -850 to 850 Hz was chosen corresponding to the PRF of MEMPHIS with ω_p equal to 300 s^{-1} and ω_0 to 100 s^{-1}. The slope of the monopulse curve depends on ω_0 and is thus directly related to the angle φ_0 between the physical channels, as stated in (25). The larger φ_0 gets, the steeper the slope of Δ/Σ. This may be of an advantage when measuring very accurate target velocities with a small Doppler shift compared to the total signal spectrum. For a mmW SAR, however, the target Doppler shift will become large because of the high carrier frequency, and a slight slope enables the exact measurement of a larger range of target velocities.

A moving target deviates from the monopulse curve of the static scene with the magnitude of deviation depending on the target's radial velocity component. This makes a moving target clearly discernible in the monopulse curve, regardless of whether the target's Doppler frequencies are inside or outside the clutter spectrum. Additionally, the monopulse curve of the static scene makes it possible to determine the Doppler shift of a target and therefore allows a correction of the azimuth displacement and estimation of the radial velocity.

B. Implementational Aspects

To be able to estimate an accurate monopulse curve $M(\omega)$ as defined in (30) from given sensor Σ and Δ signals in all samples (r, ω) and to identify moving targets, we perform the following steps which include stochastic modeling of $M(\omega)$. All these steps are executed on blocks of data split in the azimuth direction to avoid Doppler information from a too large subscene which might include multiple moving targets per range bin.

1) Because signal and SAR speckle noise may influence monopulse processing, we define an amplitude threshold T_A and consider only samples where the sum signal $|\Sigma(r,\omega)|$ is larger than the threshold with respect to the average clutter return $\overline{A}$ in decibels as

$$|\Sigma(r,\omega)| > \overline{A} \cdot 10^{T_A/20}. \tag{31}$$

2) We calculate and store the complex monopulse ratios

$$\mathrm{MPR}(r,\omega) = \Delta(r,\omega)/\Sigma(r,\omega) \tag{32}$$

over the complete Doppler spectrum for all range bins. Then, we use only the real part of this ratio (assuming a phase difference between channels of 0, see [10, Ch. 3 and 7]). The imaginary part is considered for a phase correction later [see step 6)].

3) Presuming independence of the monopulse ratio from range r, we calculate the mean values of $\mathrm{MPR}(\omega)$ over all r.

4) As shown in (30), the monopulse curve $M(\omega)$ has the form of a hyperbolic tangent. To fit a curve $M(\omega)$ through

all values MPR(ω), we assume a parameterization

$$M(\omega) = a \cdot \tanh(b\omega - c) \tag{33}$$

where a, b, and c are free parameters.

5) We estimate a, b, and c through nonlinear data modeling. A good technique is the Levenberg–Marquardt method in combination with singular value decomposition for the solution of the sets of linear equations (compare [20, Ch. 15]). For the method to work, reasonable initial values of a, b, and c must be chosen. They may easily be determined from the theoretical monopulse curve of a given SAR sensor in Fig. 6.
6) As mentioned in Section III-B, the individual receive channels of a monopulse system are separated locally from each other by a short distance, and we get a small constant phase difference between channels for static targets in addition to those phase differences caused by target movement. By estimating the imaginary monopulse ratios and their monopulse curve $M_{\mathrm{im}}(\omega)$, we adjust the phase of all monopulse ratios through a multiplication of the complex Σ and Δ signals with $e^{-j\phi}$ where

$$\phi = \operatorname{atan}\left(\frac{b_{\mathrm{im}}}{b_{\mathrm{re}}}\right) \tag{34}$$

and b_{re}, b_{im} are the b parameters of the real and imaginary monopulse curve of (33).
7) We estimate the monopulse curve again, now with the phase-corrected ratios.
8) Defining a monopulse threshold T_M, we ignore all ratios MPR(r, ω) that deviate less than the threshold from $M(\omega)$. Such a threshold may be defined in decibels with the help of the standard deviation σ of the fitted monopulse curve $M(\omega)$ as

$$\left|\frac{\Delta(r,\omega)}{\Sigma(r,\omega)} - M(\omega)\right| < \sigma \cdot 10^{T_M/20}. \tag{35}$$

9) We determine the necessary frequency shift of all remaining signals presumed to be coming from moving targets. The frequency shifts may be directly translated into radial velocities v_{r} by (1), and an azimuth position correction in the image becomes possible.

Note that more than one target in the same range bin may be present if the processed block size of images is set to be too large, complicating the algorithm because more than one Doppler shift must be extracted. This means that the parts in the Doppler spectrum after monopulse filtering have to be clustered in order to identify individual moving targets. Smaller block sizes may increase the adaptivity of the algorithm. However, if the block size is too small, estimation of the monopulse curve $M(\omega)$ may be inaccurate.

For the results presented in the following, Section VI a block size of 2048 echoes was chosen at both frequencies corresponding to slightly more than 1 s of data recording. No block contained more than one target. For targets appearing in more than one block, a target data buffer common to all blocks was used.

A further difficulty may be the Doppler centroid of the data. In Fig. 6, we have shown the theoretical Doppler spectra to be expected from a monopulse system. However, for real data, the signal peak of the sum channel may almost never be centered exactly at zero but shifted by the Doppler centroid caused by a radar azimuth look angle different from 90°. Additionally, the Doppler centroid shows a strong dependence on range, r, and often—considering the data focusing scheme—one on azimuth z, as well. A good estimation of Doppler centroid is needed to correct these shifts accurately before monopulse processing the data. Otherwise, correct estimation of the hyperbolic tangent will be impossible and static targets may be indicated as moving by the algorithm. Estimation of the Doppler centroid, especially at very high carrier frequencies such as for mmW SAR, is difficult and has to include navigational data as well as spectral estimation methods [21].

VI. Experimental Results

A. Targets in a Controlled Environment

The five target vehicles T_1 to T_5 of our experiment introduced in Section IV-B were moving down the runway with their exact positions and velocities logged by GPS receivers at 1-s intervals. Postmeasurement dGPS processing was used to increase position and velocity data to submeter accuracy. T_1, T_2, and T_3 were moving at 15 m/s on the lower side of the runway in Figs. 4 and 5 while T_4 and T_5 drove with 10 m/s along the upper border to minimize the possibility of collision.

Monopulse GMTI processing as described in Section V-B gives us the spectral results shown in Fig. 7 for 35 GHz and in Fig. 8 for 94 GHz. The plots show the estimated monopulse curve $M(\omega)$ and the monopulse ratios MPR(r, ω) at ranges r where a target is visible. Given are the spectra for the static reflector R_1 and targets T_1 moving at 15 m/s and T_4 at 10 m/s with $T_A = 10$ dB. The calculated monopulse ratios at the range bin of the reflector at the top left of the figure correspond very well to the estimated monopulse curve, indicating a static target. At the bottom left, we see that no frequency remains in the spectrum after including a monopulse threshold $T_M = 10$ dB. However, the targets T_1 (middle) as well as T_4 (right) are clearly identified via monopulse processing. Their relative frequency shifts are easily discernible once a monopulse threshold is applied.

Figs. 9 and 10 show the outcome in the time domain of our described monopulse algorithm for 35 and 94 GHz, respectively. All signal parts found to be static by monopulse processing have been filtered out in the Doppler domain before inversely Fourier transforming the remaining signal back to the time domain. For orientation purposes, the airfield runway is outlined in the figures. Obviously, the target repositioning is as sensitive as the velocity estimation. An error in the velocity estimation of $\Delta v_{\mathrm{r}} = 0.1$ m/s results in a position uncertainty of 1 m as calculated in (3), assuming an aircraft velocity of $v_{\mathrm{s}} = 100$ m/s and a range to the target of $R = 1000$ m.

All indicated targets appear in black and their calculated true ground positions in gray. The resulting velocity components in range are listed in Table I and compared with calculated

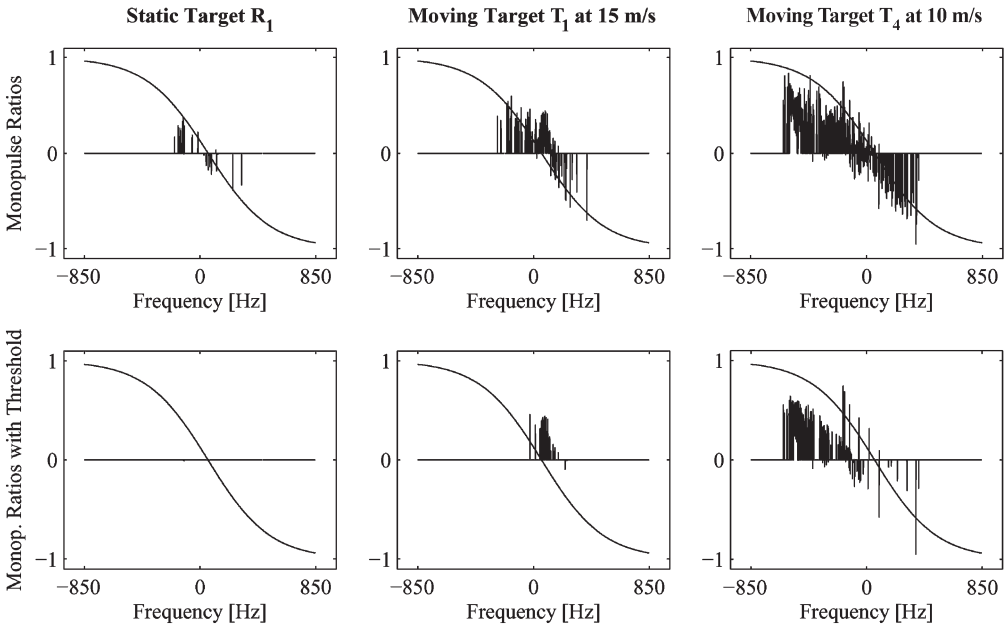

Fig. 7. Monopulse ratios at 35 GHz (top) before and (bottom) after thresholding with T_M. (Left) Ratios of a static reflector fit on the adaptively calculated monopulse curve. (Middle) Thresholding of the range bin including T_1 and (top) background clutter leaves the indication of (bottom) a moving target at 15 m/s. A positive Doppler shift is clearly discernible. (Right) Indication of T_4 moving at 10 m/s and showing a negative Doppler shift when static clutter is removed.

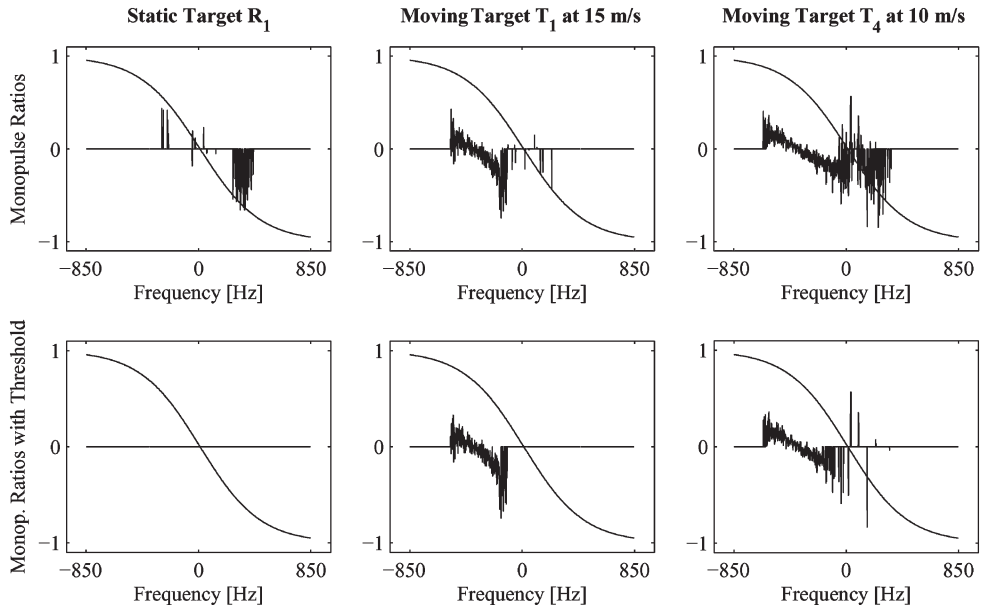

Fig. 8. Monopulse ratios at 94 GHz (top) before and (bottom) after thresholding with T_M for the same targets at the same time as in Fig. 7. (Left) Ratios of a static reflector fit on the adaptively calculated monopulse curve. (Middle) Indication of T_1 moving at 15 m/s. (Right) Indication of T_4 moving at 10 m/s.

relative velocities between the sensor and the targets obtained from dGPS data. All targets are detected at 35 GHz while at 94 GHz, T_2 experienced a blind speed at the time of illumination and the target intensity of T_5 is weak and disappears in the clutter. Even at 35 GHz, T_5 is very weak and barely indicated as a moving target. The resulting velocity estimation for T_5 is worse than that for the other targets. For T_1 to T_4, velocity estimates from the monopulse processing agree very well with dGPS measurements with no more than 3% deviation, and displacement corrections show correct target positions.

Also, in Table I, we see how the velocity measurement ambiguities indicated by the factors m and n defined in (16) can be resolved by using the dual-frequency information. We solved the system of equations (compare columns 3 and 4 in Table I) and assumed that the condition of the velocities being inside of the least common multiple velocity in (15) is fulfilled with $x = 4$. Obviously, we could not solve such a system for targets T_2 (blind speed at 94 GHz) and T_5 (weak signal at 94 GHz). For T_2, the indication from the companion frequency at 35 GHz can be used to state a blind velocity as $0 + m \cdot 2.71$ m/s. However, this approach does not work for a target that is moving with a velocity different from a blind speed but with a weak echo, such as T_5. There, the amplitude threshold of (31) or the monopulse threshold of (35) would have to be relaxed once a moving target

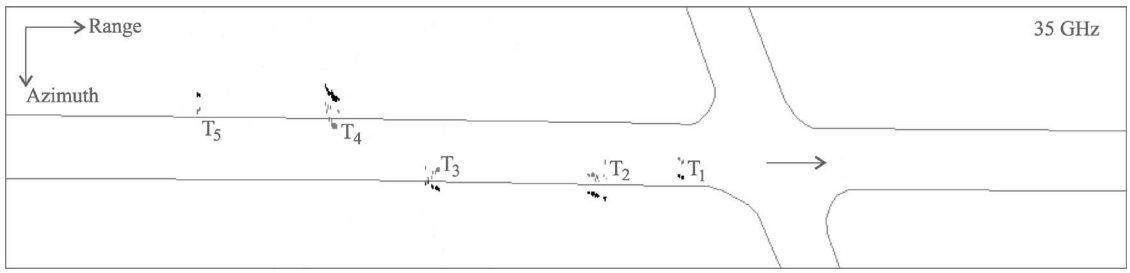

Fig. 9. Automatically indicated (black) and position-corrected (gray) moving targets at 35-GHz carrier frequency. The static corner reflectors R_1 and R_2 have correctly disappeared.

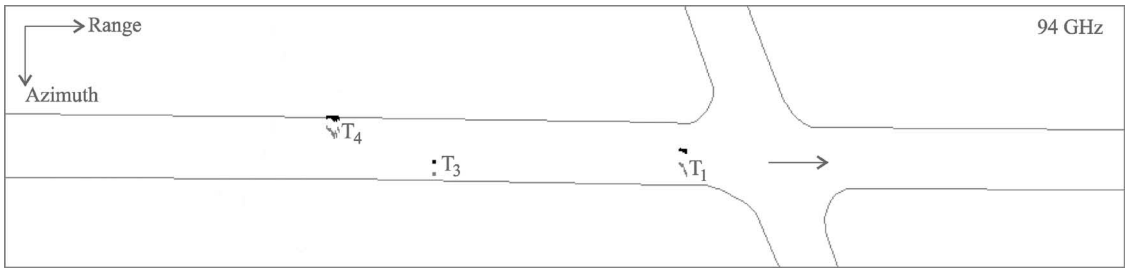

Fig. 10. Automatically indicated (black) and position-corrected (gray) moving targets at 94-GHz carrier frequency. T_2 is moving with a blind speed while T_5 is too weak to be indicated.

TABLE I
CONTROLLED ENVIRONMENT RESULTS (SEE FIGS. 9 AND 10): ABSOLUTE NOMINAL VALUES AND MEASURED RADIAL VELOCITIES OF MOVING TARGETS BY dGPS AND BY THE MEMPHIS DUAL-FREQUENCY MONOPULSE SAR SENSOR. NEGATIVE VALUES INDICATE A MOVEMENT AWAY FROM THE SAR. THE NUMBERS OF DOPPLER AMBIGUITIES m AND n ARE RESOLVED VIA LEAST COMMON MULTIPLES TO GET THE DUAL-FREQUENCY VELOCITY ESTIMATE. $\Delta\epsilon$ IS THE DEVIATION BETWEEN THE 35- AND 94-GHz VELOCITY MEASUREMENT GIVEN BY (17)

Target	Nom. Velocity (ground) [m/s]	35 GHz SAR Vel (radial) [m/s]	94 GHz SAR Vel (radial) [m/s]	m	n	$\Delta\epsilon$ [m/s]	Dual-Freq SAR Vel (radial) [m/s]	dGPS Vel (radial) [m/s]	ΔSAR-GPS [m/s]
T_1	15	$0.57 + m \cdot 7.28$	$-0.64 + n \cdot 2.71$	-2	-5	0.2	-14.1	-14.4	0.3
T_2	15	$0.66 + m \cdot 7.28$	blind	(-2)	—	—	(-13.9)	-14.0	0.1
T_3	15	$0.73 + m \cdot 7.28$	$-0.46 + n \cdot 2.71$	-2	-5	0.2	-13.9	-14.2	0.3
T_4	10	$-1.05 + m \cdot 7.28$	$-0.58 + n \cdot 2.71$	-1	-3	0.4	-8.5	-8.8	0.3
T_5	10	$-0.64 + m \cdot 7.28$	too weak	(-1)	—	—	(-7.9)	-8.7	0.8

has been detected in the companion frequency. With our *a priori* knowledge from the dGPS measurements and by assuming two convoys of similar velocities, we filled in the corresponding ambiguity factor m in parentheses and obtained a good velocity estimate.

For targets T_1, T_3, and T_4 we could determine a mean dual-frequency velocity. The deviation $\Delta\epsilon$ between the resulting ambiguity-resolved velocity at 35 and that at 94 GHz is of the same order as that one between the SAR and GPS measurements, indicating that our GMTI algorithm worked fine at both frequencies.

B. Targets on a Field Path

The success of the experiment with five targets in the controlled environment of an airfield encouraged the attempt to test the capabilities of MEMPHIS for targets in a much harder environment in 2005. A 3-m-wide field path running around the hilltop of Mont Racine in western Switzerland was chosen. This path is sometimes twisted, sometimes straight, and does not allow for a single, constant target velocity. Trees, rocks, and some huts are located in the immediate neighborhood of the path and the terrain is bumpy.

The same type of moving targets as on the airfield (see Section VI-A) was used. They are called T_6, T_7, and T_8 in the following. T_6 and T_8 were outfitted with corner reflectors and all three vehicles carried GPS equipment logging position and velocity. The target velocities were to be around 10 m/s, but were ultimately determined by path conditions and the drivers' discretion. Multiple SAR flights around the hill were planned, always with the knoll at the center. There, three reflectors R_4, R_5, and R_6 were positioned, looking perpendicular to the various planned flight tracks. As we will see, they are all three always visible in the recorded data, regardless of the look direction and serve as static reference targets.

Fig. 11 shows the focused SAR images of the field path at 35 and 94 GHz. These images have been processed with the monopulse GMTI algorithm presented in Section V-B. Unlike the results from the airfield of the previous Section VI-A, the GMTI results are directly represented as color pixels in the SAR image. Red indicates moving targets and green their true position. All signals found to be deviating from the monopulse

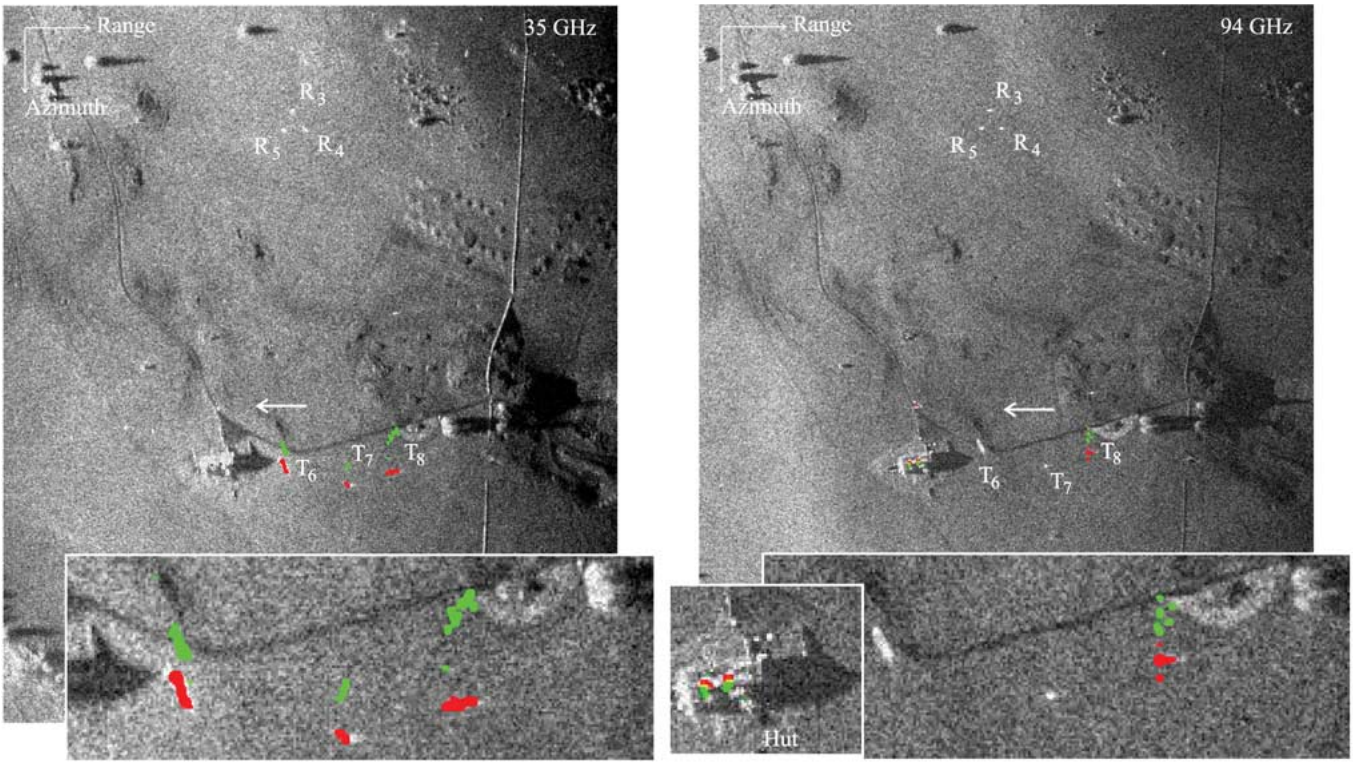

Fig. 11. Automatic indication of moving targets T_6 to T_8, moving toward the SAR sensor, with detection (red) and position correction (green) done directly in the SAR image. The targets were moving on a field path. The image dimensions are 460×540 m^2 with a resolution of 0.75 m. Enlarged at the bottom is the area of interest with the moving targets.

curve $M(\omega)$ have been marked in the Doppler domain before separately inversely Fourier-transforming the static and non-static signals back into the time domain. This gives us the advantage of having the static information of the SAR image combined with the moving target information. To give some more emphasis on small moving targets, their immediately neighboring pixels may be colored, too, as has been done in Fig. 11 and all following images of combined SAR and GMTI results.

In both, Fig. 11(a) and (b), the three static corner reflectors R_4, R_5, and R_6 are clearly visible. Since none of them is colored red, they have been correctly identified as static targets. The three moving targets T_6 to T_8 were moving toward the SAR sensor. At 35-GHz carrier frequency, the SAR image shows all three targets clearly. T_6 is moving at a greater angle relative to the sensor line of sight than the other two. Hence, its radial velocity is smaller, and its displacement in azimuth away from the path is less than for T_7 and T_8. T_7 without a corner reflector shows a weaker target signature and its GMTI corrected position is not on the path but some meters south. If we look at the 94-GHz image in Fig. 11(b), we see that T_7 is not even indicated as a target. A closer analysis shows that the brightest returns from T_7 at 94 GHz are about 8 dB above the clutter level while the GMTI algorithm only considered targets of $T_A = 10$ dB and higher [see (31)]. T_6 on the other hand, is not indicated at 94 GHz as a moving target even though its signature is very prominent. Since its signature lies exactly on the path, we deduce that it was moving at a blind speed in 94-GHz SAR. T_8 was detected as the sole moving target. Its corrected position is almost on the path.

Furthermore, and only visible when enlarged in Fig. 11(b), the hut in front of T_6 shows traces of GMTI colors on its roof when observed by the 94-GHz SAR. This is an indication for either a movement or—as a hut is unlikely to have moving parts on its roof—a misregistration in the monopulse algorithm for this particular block of data, most likely coming from a Doppler centroid estimation of the data that is not accurate [Fig. 11(b) includes six processing blocks with individual monopulse curve estimations; see Section V-B]. The second assumption would be encouraged by the very small position correction on the hut roof targets, indicating a very slow movement that could come from a monopulse curve misfit. It would also explain why the corrected position of T_8 is not located on the path. The Doppler centroid at different data blocks, for example at the static corner reflectors in mid range, does not show any misregistration. Hence, another possibility may be that the range dependence of the Doppler centroid is not estimated correctly and the values are only inaccurate in near range. Most probable, however, is the assumption that metallic parts on the hut roof have saturated the SAR receive channels, resulting in incorrect phase recordings.

In Table II, the target velocities are shown as evaluated by dGPS and by GMTI processing. Because T_7 is too weak and T_6 was moving at a blind speed in Fig. 11(b), their true radial dual-frequency velocity could only be calculated with the information from the dGPS data and have been put in parentheses.

TABLE II
FIELD PATH RESULTS FOR PERPENDICULAR TARGET MOVEMENT (SEE FIG. 11): MEASURED RADIAL VELOCITIES BY dGPS AND BY MEMPHIS. THE NUMBERS OF DOPPLER AMBIGUITIES m AND n ARE RESOLVED VIA LEAST COMMON MULTIPLES TO GET THE DUAL-FREQUENCY VELOCITY ESTIMATE. $\Delta\epsilon$ IS THE DEVIATION BETWEEN THE 35- AND 94-GHz VELOCITY MEASUREMENT GIVEN BY (17)

Target	Nom. Velocity (ground) [m/s]	35 GHz SAR Vel (radial) [m/s]	94 GHz SAR Vel (radial) [m/s]	m	n	$\Delta\epsilon$ [m/s]	Dual-Freq SAR Vel (radial) [m/s]	dGPS Vel (radial) [m/s]	ΔSAR-GPS [m/s]
T_6	10	$0.85 + m \cdot 7.28$	blind	(1)	—	—	(8.1)	8.3	0.2
T_7	10	$0.76 + m \cdot 7.28$	too weak	(1)	—	—	(8.0)	9.5	1.5
T_8	10	$1.68 + m \cdot 7.28$	$0.74 + n \cdot 2.71$	1	3	0.0	8.9	9.1	0.2

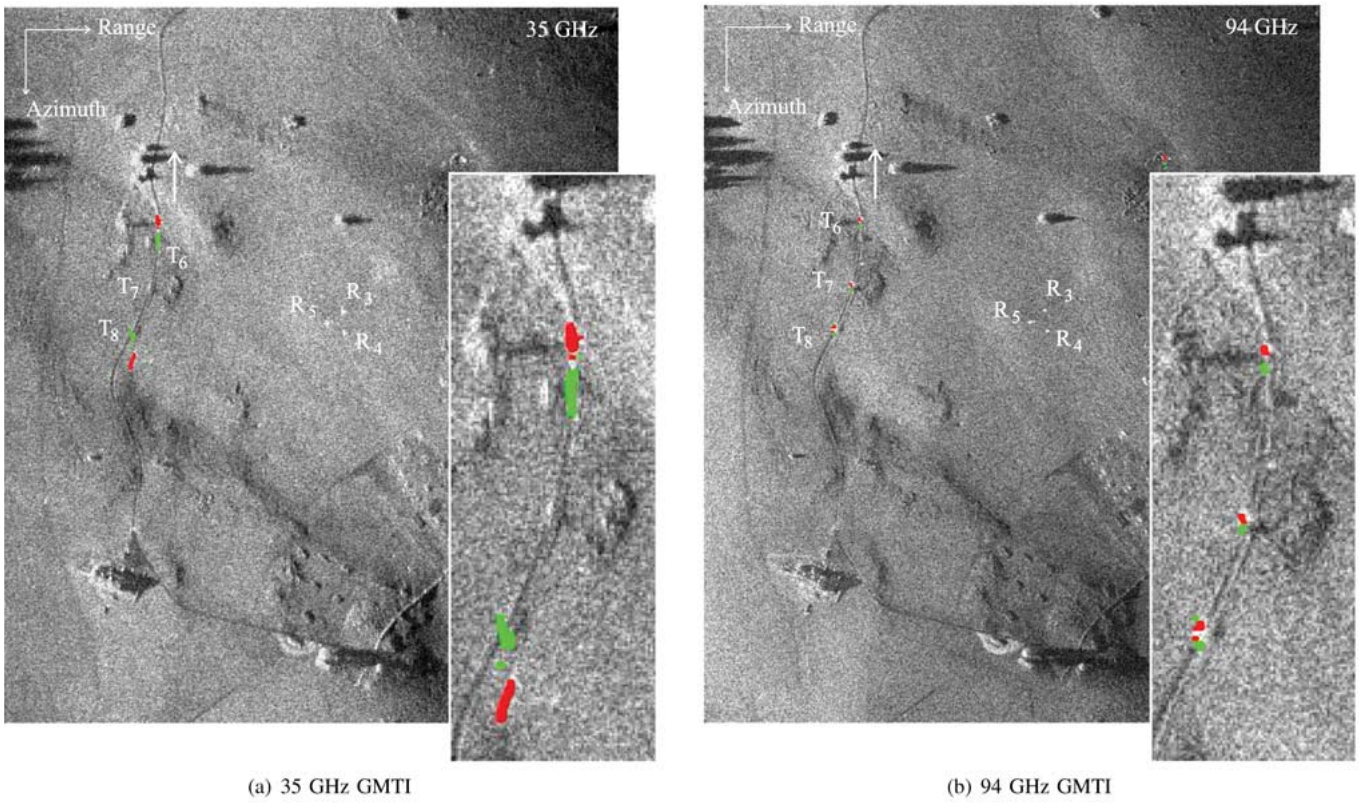

(a) 35 GHz GMTI (b) 94 GHz GMTI

Fig. 12. Automatic indication of moving targets T_6 to T_8, moving parallel and in opposite direction to the SAR sensor, with detection (red) and position correction (green) done directly in the SAR image. The targets were moving on a field path. The image dimensions are 460×540 m^2 with a resolution of 0.75 m. Enlarged on the right side is the area of interest with the moving targets.

TABLE III
FIELD PATH RESULTS FOR PARALLEL TARGET MOVEMENT (SEE FIG. 12): ABSOLUTE NOMINAL VALUES AND MEASURED RADIAL VELOCITIES OF MOVING TARGETS BY dGPS AND BY THE MEMPHIS DUAL-FREQUENCY MONOPULSE SAR SENSOR. NEGATIVE VALUES INDICATE A MOVEMENT AWAY FROM THE SAR. THE NUMBERS OF DOPPLER AMBIGUITIES m AND n ARE RESOLVED VIA LEAST COMMON MULTIPLES TO GET THE DUAL-FREQUENCY VELOCITY ESTIMATE. $\Delta\epsilon$ IS THE DEVIATION BETWEEN THE 35- AND 94-GHz VELOCITY MEASUREMENT GIVEN BY (17)

Target	Nom. Velocity (ground) [m/s]	35 GHz SAR Vel (radial) [m/s]	94 GHz SAR Vel (radial) [m/s]	m	n	$\Delta\epsilon$ [m/s]	Dual-Freq SAR Vel (radial) [m/s]	dGPS Vel (radial) [m/s]	ΔSAR-GPS [m/s]
T_6	10	$-1.19 + m \cdot 7.28$	$-1.10 + n \cdot 2.71$	0	0	0.0	-1.2	-1.2	0.0
T_7	10	too weak	$-0.66 + n \cdot 2.71$	—	(-1)	—	(-3.4)	-3.7	0.3
T_8	10	$1.56 + m \cdot 7.28$	$-0.69 + n \cdot 2.71$	-1	-2	0.2	-5.9	-5.4	0.5

In addition, the data shows that the two strong targets T_6 and T_8 have very precise velocity estimations compared with the dGPS data while the velocity of the weaker target T_7 could not be estimated as accurately.

A second dual-frequency SAR imagery pair from the same experiment is shown in Fig. 12. The flight track was slightly different and the targets T_6 to T_8 were moving on a different section of the field path. This caused the constellation between SAR flight track and targets to be almost parallel, but in opposite directions. Such a situation is the most difficult for a GMTI algorithm designed to detect radial velocities. However, as may be seen in the imagery and confirmed in Table III, monopulse processing works even in this difficult situation where radial target velocities are extremely small.

At 35 GHz in Fig. 12(a), targets T_6 and T_8 are detected as moving and their shifted SAR positions are corrected. T_7 either has too weak a signature to be detected or is moving with a too low radial velocity. At 94 GHz in Fig. 12(b), all targets are detected and their position is corrected. This shows that T_7 has a radial velocity, and it is its signature in the 35-GHz image that prevents indication there. A close analysis shows that the brightest returns from T_7 at 35 GHz are about 7 dB above the clutter level while the GMTI algorithm only considered targets of $T_A = 10$ dB and higher.

All three control targets, the corner reflectors R_4, R_5, and R_6 are perfectly visible in the image. None of them is colored, showing correct GMTI processing. A noticeable difference between the two images at 35 and 94 GHz in Fig. 12 is target smearing. At 35 GHz, the two visible targets are smeared significantly. The nonvisibility of target T_7 may even be caused by this smearing. At 94 GHz, where the synthetic aperture of MEMPHIS is only about half as long as at 35 GHz and a target is illuminated by the SAR for a shorter time, the smearing is small. Targets are focused and with a clear signature. This is a significant advantage of a smaller synthetic aperture as discussed in Section II.

On the other hand, small, nonsmeared targets also present a disadvantage. While T_6 and T_8 in Fig. 12(a) at 35 GHz include almost 300 individual single-look complex image pixels, they are made up of only 30 to 50 pixels in Fig. 12(b) at 94 GHz. This may reduce detectability considerably, especially if one would try to extend a GMTI algorithm with a threshold on target size and discard very small detected targets as phase disturbances, wind in trees, insufficient motion compensation of the SAR sensor movement, or many more effects influencing GMTI, including different look angles of the independent monopulse beams of the system [see Fig. 2(a)] and speckle.

C. Targets on a Freeway

A last experiment, that was also conducted in western Switzerland in 2005, included dual-frequency monopulse data collected over a freeway. The aim was to measure fast moving targets of opportunity on roads. Conclusions from this experiment give valuable information on traffic monitoring capabilities of mmW SAR.

Because a reference measurement on the ground was desirable to control GMTI SAR measurements, a team from the Swiss Federal Office of Metrology (METAS) was responsible for ground-based radar and laser measurements of targets moving southward on the freeway and automatically taking photographs with time stamps and velocities of all measured vehicles.

GMTI results show the 35 and 94-GHz SAR images from a recorded track in Fig. 13(a) and (b) where two large trucks are visible. They are colored red because they are correctly indicated by monopulse processing as moving and their calculated position shifts are given in green. When there are cases where an indicated target overlaps with a corrected position of the same or another target, the color used is yellow. Hence, the trucks were colored using the same method as in the previous experiment of Section VI-B, where monopulse results and the static SAR image are fused to form a single image. We call the trucks, which were both moving southward, T_9 and T_{11}. Another clearly visible target moving in the opposite direction is designated as T_{10}. There are two static corner reflectors R_6 and R_7 present in the data sets. They serve as reference and control targets for the GMTI algorithms.

The flight heading to create the image in Fig. 13 was chosen as a compromise. For traffic monitoring, one would like to have a section of the road in the data that is as large as possible. This implies a flight heading parallel to the freeway. For GMTI, radial velocities are the largest for a flight track across the freeway. Finally, for an optimal radar cross section of targets, imaging from the side or from the front is optimal [22], requiring a flight track either parallel to or across the freeway. The chosen compromise consisted of a flight track at 20° to the freeway. This means that a large section of the freeway was included in the image. It also means that imaging of targets nearly from the side caused only a minimum reduction of their radar cross section while there would be a measurable radial target velocity. The main drawback would be the large target smearing because of the almost parallel movement with the SAR (see Section II) or, if the targets were moving in opposite direction to the SAR, a very short illumination time.

With the given flight heading relative to the freeway and the exact depression angles, measured radial target speeds may be converted to true ground velocities on the road. A dual-frequency GMTI analysis resulted in a ground velocity of 21.1 m/s for T_9 and one of 23.9 m/s for T_{11} with $\Delta\epsilon$ equal to 0.3 m/s (T_9) and 0.2 m/s (T_{11}). T_{10} was moving in the opposite direction at 25.0 m/s and $\Delta\epsilon$ equal to 0.1 m/s. Ground-based radar and laser measured T_9 moving at 22.5 m/s and T_{11} at 23.9 m/s. The northward moving T_{10} was not measured on the ground. As a quality control, it may be observed that both corner reflectors R_6 and R_7 were identified as static targets.

The ground measurements were done near the bridge visible in Fig. 13, directly opposite to the indicated target T_{10}. This means that the velocity measurements of T_{11} happened within around 2 s, and hence almost simultaneously, for both, the SAR and the ground-based radar. The difference between the two measurements is zero. The measurement of T_9 by the SAR was about 10 to 15 s earlier than the one on the ground. The two measurements differ by 1.4 m/s. This could well be because of a target slow down. After all, the ground-based measurement installation was well visible from the road and would have caused most drivers to slow down slightly, be it due to curiosity or precaution.

T_9 and T_{11} could both be identified by the available photographs as trucks. However, in between the two trucks, two additional small cars were passing the ground measurement installation and were photographed. Their target signature could not be detected by the GMTI algorithm. Neither is their signature visible in the SAR images. The two cars were small and the fast movement parallel to the SAR must have caused such a large smearing and defocusing that they simply disappear in the clutter.

South of the bridge, there are two very slight and smeared signatures visible on the right side of the freeway in both,

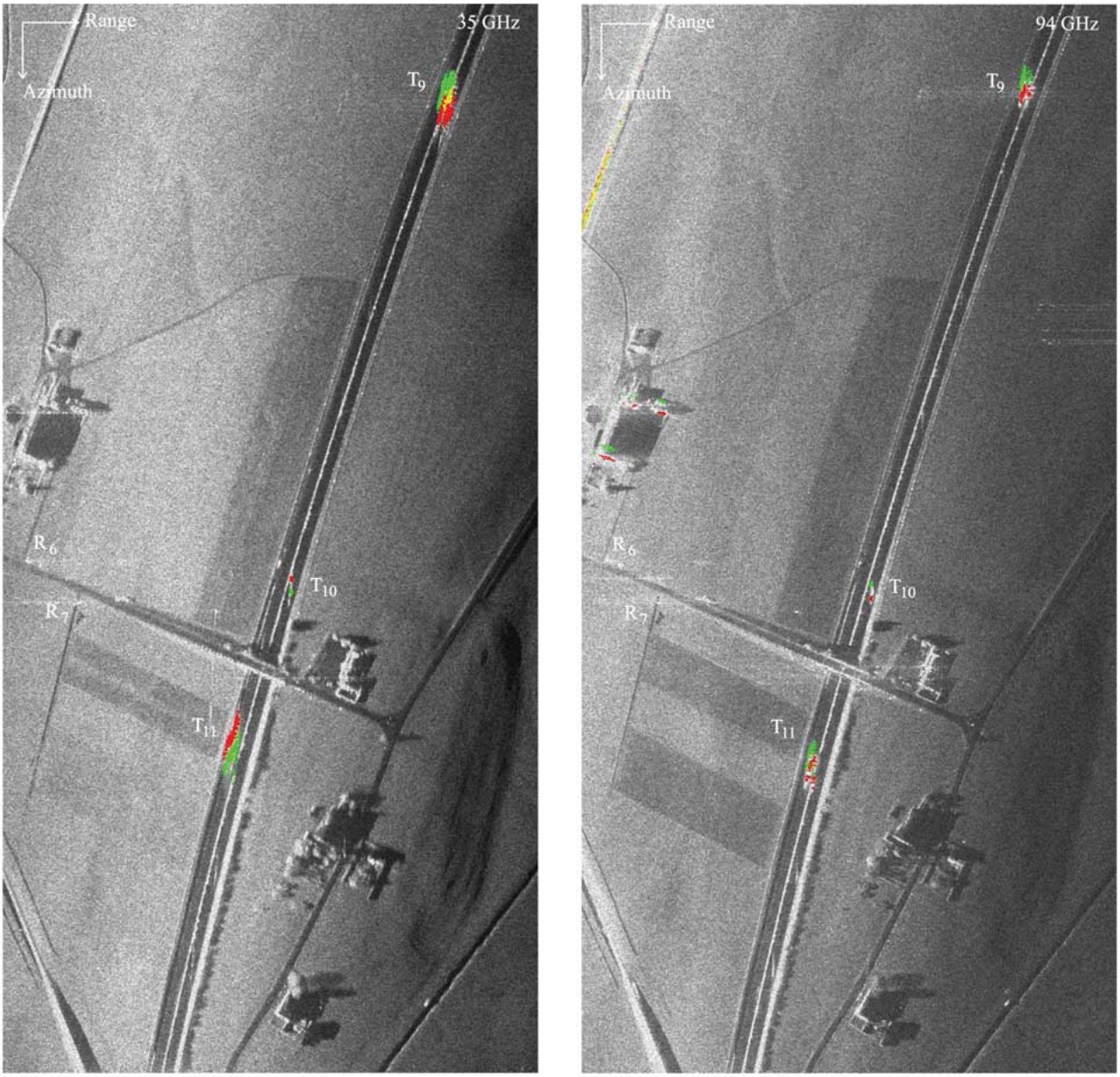

Fig. 13. Automatic indication of moving targets T_9 to T_{11} moving on a freeway, with detection (red) and position correction (green) done directly in the SAR image. Yellow areas exist where a detected target overlaps with a position-corrected one. The image dimensions are 500×1000 m^2 with a resolution of 0.75 m.

Fig. 13(a) and (b). They are probably two cars moving northward. They are not indicated by GMTI because their smeared signatures are too weak for extraction.

Finally, there are disturbances visible on a building in Fig. 13(b), directly above the corner reflector R_6, and also on the railway tracks visible just below the geometry indication of range and azimuth in the top left corner. This is the same 94-GHz phenomenon discussed in the previous Section VI-B. Some GMTI processed data blocks may have experienced an insufficiently accurate Doppler centroid estimation in near range or an inaccurate monopulse curve estimation (Fig. 13(b) was GMTI processed with 12 blocks of independent monopulse curve estimations). Alternatively, sensor saturation may have caused incorrect phase recordings. The rest of the scene is processed correctly: the same railway track, falsely indicated in the north is also visible in the south at the bottom left corner and is indicated as static. Other buildings in center and far range, the corner reflectors, and also the bright freeway center guard rails are indicated as static.

D. Discussion

The three experiments of Sections VI-A–C highlight the capabilities of GMTI with a mmW SAR. They demonstrate good target detectability for slow-moving targets and also for large fast moving ones. However, if targets have a high velocity parallel to the SAR and a small radar cross section as the cars on a freeway do, they may disappear. Adequate radar cross

section is crucial in all experiments. Moving targets with corner reflectors show larger GMTI signatures and better velocity estimates and position correction.

For all three experiments, an amplitude threshold of 10 dB above the clutter level [see (31)] and also a monopulse threshold of 10 dB [see (35)] were used. Higher values suppressed too much information of targets and target movements. Lower values added disturbances from various sources such as phase disturbances from motion compensation and aircraft movement, effects of clutter movement by wind, or possibly target signature variations from different aspect angles by the squinted monopulse beams and speckle.

Important additional information on the quality of a GMTI outcome may be drawn from the number of pixels in an image. A single pixel being indicated as moving may well be caused by speckle or phase disturbances while several hundred clustered pixels provide a reliable moving target indication. This opens the possibility to include a filter based on target size to improve on a constant false alarm rate (CFAR) instead of the simple threshold used. A direct analysis of CFAR performance would be beyond the scope of this paper, and the reader is referred to [23].

Furthermore, the presented GMTI algorithm is based on a theory assuming constant target velocity. Results on field paths, where targets necessarily had to break in bends and due to path conditions and then accelerate again, showed good results and no recognizable influence from such small nonconstant movement effects. For an analysis of large target acceleration, see [24] and [25].

Finally, change detection between the two images of a dual-frequency SAR may offer an additional help to decide on the indication of moving targets. A hut roof in Fig. 11(b) and railway tracks in Fig. 13(b) are indicated as moving at 94 GHz but not at 35 GHz. Change detection may be a unreliable technique, though, because target and clutter radar cross section may vary greatly, as may be seen by the frequency-dependent reflectivity of fields near target T_{11} in Fig. 13(a) and (b).

VII. Conclusion

For mmW SAR systems, amplitude-comparison monopulse data collection is a very effective GMTI recording technique that solves the dilemma of extremely short interferometric mmW baselines. It is a sound method with multiple channels sharing a single phase center. The basic concept is well known from tracking radar applications and directly transferable to SAR GMTI scenarios.

Processing of monopulse data for SAR GMTI includes the mathematically complex nonlinear data modeling step presented in this paper to fit received and compressed signals to a stochastically determined hyperbolic tangent function in the range Doppler domain. Resulting deviations of moving targets from this function and thus from the static scene are easily detectable and corrected, allowing for exact radial target velocity calculations and position shift corrections.

When calculating radial target velocities, a general problem for mmW SAR GMTI are high-Doppler-frequency shifts from the detected targets even at velocities of a few meters per second. PRF requirements for unambiguous velocity measurements would be exceedingly high. Using dual-frequency information, the concern about high PRF requirements is eliminated using the theory of least common multiples of the single-velocity ambiguities. Indication of targets is very sensitive, and accurate position corrections are possible.

Experimental data were presented, recorded with the dual-frequency 35- and 94-GHz SAR system MEMPHIS. GMTI results obtained with the presented processing algorithm showed the effectiveness of monopulse processing for SAR and the capabilities in different environments and with various radial and tangential target velocities. Monopulse processing of the Δ/Σ Doppler signal ratios made use of complex signal information to estimate and generate a phase-corrected monopulse curve. Velocity estimates and target displacement correction were accurate and could be fully automated using blockwise monopulse processing of large SAR scenes. Additional considerations and possibilities of dual-frequency SAR for GMTI were discussed, including target blind speed elimination and change detection.

Important for the GMTI performance in all target environments and for all target velocities proved to be accurate, range-dependent Doppler centroid values as well as suppression of phase disturbances from motion compensation and aircraft movement, influences of clutter movement by wind, and speckle variations from different look angles of the monopulse beams by amplitude and monopulse thresholding. We could show that the theoretical hyperbolic tangent monopulse curve fits very well to measured static corner reflector data, giving proof to the practical application of our modeling approach and also to the theory of dual-frequency SAR.

Acknowledgment

The authors would like to thank M. Hägelen (FGAN-FHR) for the many inputs and ideas. Furthermore, we would also like to thank the procurement and technology center of the Swiss Federal Department of Defense (armasuisse), especially P. Wellig and K. Schmid, for their wide support and cooperation. The commitment of H. Essen and his MEMPHIS team at FGAN and of the C-160 flight crew from WTD-61 has rendered possible the realization of the presented experiments. Special thanks are due to E. Brülhart, M. Wollensack, and W. Fasel [Swiss Federal Office of Metrology (METAS)] for valuable ground truth measurements.

References

[1] R. K. Raney, "Synthetic aperture imaging radar and moving targets," *IEEE Trans. Aerosp. Electron. Syst.*, vol. AES-7, no. 3, pp. 499–505, May 1971.

[2] S. R. J. Axelsson, "Position correction of moving targets in SARImagery," *Proc. SPIE*, vol. 5236, pp. 80–92, Jan. 2004.

[3] S. Chiu and C. E. Livingstone, "A comparison of displaced phase centre antenna and along-track interferometry techniques for RADARSAT-2 ground moving target indication," *Can. J. Remote Sens.*, vol. 31, no. 1, pp. 37–51, Feb. 2005.

[4] C. Liu, "Effects of target motion on polarimetric SAR images," *Can. J. Remote Sens.*, vol. 32, no. 2, pp. 51–64, Apr. 2006.

[5] R. Romeiser, H. Breit, M. Eineder, H. Runge, P. Flament, K. de Jong, and J. Vogelzang, "Current measurements by SAR along-track interferometry from a space shuttle," *IEEE Trans. Geosci. Remote Sens.*, vol. 43, no. 10, pp. 2315–2324, Oct. 2005.

[6] J. H. G. Ender, "Space-time processing for multichannel synthetic aperture radar," *Electron. Commun. Eng. J.*, vol. 11, no. 1, pp. 29–38, Feb. 1999.
[7] J. Ward, "Space-time adaptive processing for airborne radar," Lincoln Lab., MIT, Lexington, MA, Tech. Rep. 1015, Dec. 1994.
[8] A. Farina and P. Lombardo, "Space-time techniques for SAR," in *Applications of Space-Time Adaptive Processing*, R. Klemm, Ed. London, U.K.: Inst. Electr. Eng., 2004, pp. 73–122.
[9] M. Soumekh, "Moving target detection and imaging using an X-band along-track monopulse SAR," *IEEE Trans. Aerosp. Electron. Syst.*, vol. 38, no. 1, pp. 315–333, Jan. 2002.
[10] S. M. Sherman, *Monopulse Principles and Techniques*. Boston, MA: Artech House, 1984.
[11] M. Rüegg, M. Hägelen, E. Meier, and D. Nüesch, "Moving target indication with dual frequency millimeter wave SAR," in *Proc. IEEE Conf. RADAR*, Verona, Italy, Apr. 2006, pp. 350–357.
[12] H. Schimpf, H. Essen, S. Böhmsdorff, and T. Brehm, "MEMPHIS—A fully polarimetric experimental radar," in *Proc. IGARSS*, Toronto, ON, Canada, Jun. 2002, vol. 3, pp. 1714–1716.
[13] M. Soumekh, "Synthetic aperture radar signal processing with MATLAB algorithms," in *Moving Target Detection and Imaging*. New York: Wiley, 1999, ch. 6.7, pp. 465–477.
[14] L. Armijo, "A theory for the determination of wind and precipitation velocities with Doppler radars," *J. Atmos. Sci.*, vol. 26, no. 3, pp. 570–573, May 1969.
[15] R. J. Doviak, D. S. Zrnic, and D. S. Sirmans, "Doppler weather radar," *Proc. IEEE*, vol. 67, no. 11, pp. 1522–1553, Nov. 1979.
[16] D. P. Jorgensen, T. R. Shepherd, and A. S. Goldstein, "A dual-pulse repetition frequency scheme for mitigating velocity ambiguities of the NOAA P-3 airborne Doppler radar," *J. Atmos. Ocean. Technol.*, vol. 17, no. 5, pp. 585–594, May 2000.
[17] G. Corsini, M. Diani, F. Lombardini, and G. Pinelli, "Simulated analysis and optimization of a three-antenna airborne InSAR system for topographic mapping," *IEEE Trans. Geosci. Remote Sens.*, vol. 37, no. 5, pp. 2518–2529, Sep. 1999.
[18] R. Bamler, "A comparison of range-Doppler and wavenumber domain SAR focusing algorithms," *IEEE Trans. Geosci. Remote Sens.*, vol. 30, no. 4, pp. 706–713, Jul. 1992.
[19] B. R. Mahafza and A. Z. Elsherbeni, "Matlab simulations for radar system design," in *Target Tracking*. Boca Raton, FL: CRC, ch. 9, pp. 401–470.
[20] W. H. Press, B. P. Flannery, S. A. Teukolsky, and W. T. Vetterling, *Numerical Recipes in C: The Art of Scientific Computing*, 2nd ed. Cambridge, U.K.: Cambridge Univ. Press, 1992.
[21] I. G. Cumming and F. H. Wong, "Digital processing of synthetic aperture radar data," in *Doppler Centroid Estimation*. Boston, MA: Artech House, 2005, ch. 12, pp. 481–565.
[22] G. Palubinskas, H. Runge, and P. Reinartz, "Radar signatures of road vehicles: Airborne SAR experiments," *Proc. SPIE*, vol. 5980, pp. 60–70, Sep. 2005.
[23] C. H. Gierull, "Statistical analysis of multilook SAR interferograms for CFAR detection of ground moving targets," *IEEE Trans. Geosci. Remote Sens.*, vol. 42, no. 4, pp. 691–701, Apr. 2004.
[24] J. J. Sharma, C. H. Gierull, and M. J. Collins, "The influence of target acceleration on velocity estimation in dual-channel SAR-GMTI," *IEEE Trans. Geosci. Remote Sens.*, vol. 44, no. 1, pp. 134–135, Jan. 2006.
[25] M. Rüegg, E. Meier, and D. Nüesch, "Constant motion, acceleration, vibration, and rotation of objects in SAR data," *Proc. SPIE*, vol. 5980, pp. 48–59, Oct. 2005.

Maurice Rüegg (S'00) received the M.Sc. degree in electrical engineering from the Swiss Federal Institute of Technology, ETH Zurich, Switzerland, in 2003. He is currently working toward the Ph.D. degree in microwave remote sensing, focusing on analyzing effects of and detection techniques for ground moving targets in SAR and millimeter wave radar data, at the Remote Sensing Laboratories, University of Zurich, Zurich.

His research interests include imaging algorithms for various air- and spaceborne SAR sensors, SAR ground moving target indication, and high-resolution SAR systems with image resolutions in the decimeter range.

Erich Meier received the M.Sc. degree in geography and the Ph.D. degree (Hons.) in remote sensing, both from the University of Zurich, Zurich, Switzerland, in 1982 and 1989, respectively.

From 1979 to 1982, he was a Research Assistant with the Remote Sensing Section and from 1982 to 1983 with the Geographic Information System Laboratory, Department of Geography, University of Zurich. From 1983 to 2006, he was a Research Scientist with the Remote Sensing Laboratories, University of Zurich where he is currently a Research Section Head involved in teaching as well as in research in digital image processing, software development for computer graphics as well as radiometric and geometric calibration of SAR and optical imagery. Since 2000, he has been the Head of the SARLab, a research group within RSL. The main research interests of this group are the development of new focusing algorithms for SAR data from UHF to millimeterwave, interferometry, polarimetry, and moving target indication algorithms as well as calibration and validation activities for spaceborne and airborne systems. He is responsible for the research strategies as well as the organization of the team. He is consultant on behalf of several national and international organizations and private companies.

Daniel Nüesch (M'82) received the M.S. degree in cartography and the Ph.D. degree in remote sensing, from the University of Zurich, Zurich, Switzerland, in 1972 and 1976, respectively.

In 1977–1978, he was a European Space Agency (ESA) Fellow at the Environmental Research Institute of Michigan (ERIM), Ann Arbor, performing NASA contract work in particular, including Landsat TM spectral band simulations and thermal infrared studies for mapping general rock types from space. From 1980 to 1982, on his second stay at ERIM, he was involved in several microwave projects such as investigations of augmenting Landsat MSS data with Seasat SAR imagery for agricultural inventories and sea ice studies. Since 1982, he has been working as a Research Scientist with the Remote Sensing Laboratories, University of Zurich, Zurich, involved in teaching and leading a large research group dedicated in particular to geometric and radiometric SAR calibration. As Scientific Division Head and Professor with the University of Zurich, he graduated 12 Ph.D. and supervised numerous postdoctoral students. As Principal and Coinvestigator, and Head of ESA's Expert Support Laboratory, he was involved in several ESA investigations for ERS-1/2 and Envisat. Since 1980, he has served as Swiss delegate to the ESA in the Data Operations Scientific and Technical Advisory Group and in the Earth Observation Programme Board. He is a member of the Swiss Federal Space Affairs Commission as well as its Prodex Programme Committee. Since June 2006, he has been in retirement.